Separation of P Phase and Fe Phase in High Phosphorus Oolitic Iron Ore by Ultrafine Grinding and Gaseous Reduction in a Rotary Furnace

JINTAO GAO, LEI GUO, and ZHANCHENG GUO

Due to the oolitic structure of the high phosphorus iron ore and the closely wrapping of apatite and hematite phases, an approach using jet mill was utilized to grind the ore to ultrafine 0.01 to 0.001 mm, which realizes the dissociation of apatite phase and hematite phase. Then in a laboratory scale rotary furnace, high phosphorus ores of different sizes were reduced by reducing gas at sub-melting point temperatures (973 to 1173 K [700 to 900 °C]). In the rotating inclined reactor, the ore particles reacted with the reducing gas coming from the opposite direction in a rolling and discrete state, which greatly improved the kinetic conditions. In this study, the reaction rate increases significantly with the decrease of particle size. For the ultrafine high phosphorus iron ores, the metallization ratio can reach 83.91 to 97.32 pct, but only 33.24 to 40.22 pct for powders with the size of 0.13 to 0.15 mm. The reduced particles maintained their original sizes, without the presence of sintering phenomenon or iron whisker. Hence, two kinds of products were easily obtained by magnetic separation: the iron product with 91.42 wt pct of Fe and 0.19 wt pct of P, and the gangue product with 13.77 wt pct of Fe and 2.32 wt pct of P.

DOI: 10.1007/s11663-015-0400-4

I. INTRODUCTION

WITH the gradual decrease of high grade iron ore reserves around the world, its supply has become the bottleneck to restrict the development of iron and steel industry. To solve the crisis of resources, utilization of the refractory ores is in an urgent need, such as the high phosphorus iron ore in massive reserves. The high phosphorus iron ore is a typical complex resource, which contains a high content of iron, but it is hard to be used due to the presence of phosphorus and its special oolitic structure.[1–3] In high phosphorus iron ore, the apatite phase and hematite phase are so intimately intermixed,[4,5] which makes it hard to grind the ore to a fine enough size to separate iron oxides and phosphorous containing phase by the conventional mechanical crushing methods.[6,7] In recent years, Omran *et al.*[8–11] have widely investigated the influence of microwave heating on the structureand the separation of phosphorus and magnetic properties of high phosphorus oolitic iron ores; the results show that microwave treatment improves phosphorus separation and magnetic properties, and consumes considerably less energy compared with the conventional thermal treatment.

For the utilization of high phosphorus oolitic iron ore, many hydrometallurgical and pyrometallurgical processes were proposed. The hydrometallurgical processes for the dephosphorization of high phosphorus iron ores mainly include the reverse flotation process,[12,13] the bioleaching process,[14–17] the acid leaching process,[18,19] and the alkaline leaching process.[20] Chemical leaching is a typical hydrometallurgical process for the dephosphorization through different acid leaching methods, and the phosphorus can be removed with little dissolution of iron and acid consumption at optimum conditions.[1,21,22] Ionkov[23] has further investigated the beneficiation routes aimed at dephosphorization of oolitic gravity magnetic concentrates, and involving a combination of roasting, re-grinding, magnetic separation, and water and acid leaching, he found that cement phases coat the oolites and penetrate inside the cracks, and goethite is partly transformed to magnetite by alkaline roasting; further by grinding to a mean size of 0.04 mm, with water and acid leaching and double magnetic separation, the phosphorus content can be decreased from 0.71 to 0.05 wt pct. The pyrometallurgical processes are beneficial for the production of direct reduction iron (DRI). Coal-based reduction is one of the typical pyrometallurgical processes by ore-carbon reduction composite agglomerates in a semi-molten state, which is always assisted with grinding and magnetic separation to separate iron and other gangue phases.[24,25] Li[26] studied the coal-based reduction of oolitic iron ore with phosphorus content of 0.24 wt pct and followed by wet milling and magnetic separation, the extracted iron has an iron grade of 92.53 wt pct. However, when the reduction temperature is above 1471 K (1198 °C), the elemental P in apatite phase will be reduced by the carbon and incorporated into metal iron. Matinde[21,22], Bai[27], and Yu[28] have investigated the dephosphorization effect by adding $Ca(OH)_2$ or Na_2CO_3 agent on the coal-based reduction;

JIN-TAO GAO, Lecturer, LEI GUO, Doctoral Student, and ZHAN-CHENG GUO, Professor, are with the State Key Laboratory of Advanced Metallurgy, University of Science and Technology Beijing, P.R. China. Contact e-mail: zcguo@ustb.edu.cn
Article published online June 22, 2015.
Manuscript submitted March 1, 2015.
Article published online July 22, 2015.

the results show that most of the Fe in the ores forms metallic state, and the additives are definitely beneficial for the dephosphorization. The gas-based reduction combined with melt separation is another typical pyrometallurgical process. Tang and Guo[29–31] adopted gaseous reduction at a temperature less than 1273 K (1000 °C) for high phosphorus iron ore powders in size mof 0.11 to 0.15 mm, which can reach a high reduction extent of iron oxide with P still in apatite. Then the reduction products were further melted at 1823 K (1550 °C), and the molten iron and slag can be separated, while about 0.2 to 0.3 wt pct of P remains in the iron and needs to be further removed.[32] As for the transformation and transmission mechanism of phosphorus during melt separation process, Tang[29–31] considered that the P exists in the melt as apatite inclusions. Fukagai[32] has studied the reaction of the $2CaO{\cdot}SiO_2$ and FeO_x-CaO-SiO_2-P_2O_5 slag at 1573 K (1300 °C), and reported that the CaO-SiO_2-P_2O_5 solid phases with high P_2O_5 content were surrounded with coexisting phases of FeO-CaO-SiO_2 system without P_2O_5.

In this paper, an approach was utilized to grind the high phosphorus iron ore to ultrafine 0.01 to 0.001 mm by using the jet mill, which will be beneficial for the dissociation of apatite phase and hematite phase. Then in a laboratory scale rotary furnace, the ore powders with different sizes (d_1 = 0.15 to 0.13 mm, d_2 = 0.13 to 0.11 mm, d_3 = 0.11 to 0.10 mm, d_4 = 0.10 to 0.09 mm, d_5 = 0.09 to 0.07 mm, d_6 < 0.07 mm, d_7 = 0.01 to 0.001 mm) were reduced at sub-melting point temperatures (973 to 1173 K [700 to 900 °C]) using the reformed blast furnace gas as reducing gas; the apatite will not be reduced nor smelted into the iron phase in this temperature range. Hence, the magnetic separation of reduction product was further carried out.

II. EXPERIMENTS

A. *Material*

The high phosphorus iron ore in Hubei Enshi was selected as the raw material. Its chemical compositions are shown in Table I, in which the mass fraction of Fe and P are 44.04 and 0.80 wt pct, respectively. The mineralogical compositions are shown in Figure 1, which mainly includes hematite, quartz, and apatite.

By using a DMRX polarizing microscope, the micro structure can be observed as shown in Figure 2. According to SEM-EDS analyses shown in Table II, it can be seen that the high phosphorus iron ore mineral is mainly in the oolitic structure in size of 0.2 to 0.5 mm. It mainly comprises hematite phase (see Figure 2: H_1 to H_4), and $Al_4[Si_4O_{10}](OH)_8$ coexisting with the hematite phase (see Figures 2(b) and (c): C_1, C_2), as well as quartz phase connecting with oolitic unit with irregular shape in the size of 0.1 to 0.3 mm (see Figure 2(b): Q_1, Q_2). The P and Ca exist in the form of fluorapatite ($Ca_5[PO_4]_3F$), whose size is only 0.001 to 0.01 mm, and heterogeneously distributed among the oolitic unit (see Figure 2(a): A_1, A_2) or in the oolitic layers (see Figures 2(b) and (C): A_3, A_4,). Moreover, the distance between apatite containing mineral layer and hematite containing mineral layer is only a few microns. Obviously, by conventional mechanical grinding it is difficult to realize the physical dissociation of apatite phase and hematite phase.

B. *Experimental Procedure*

(1) Dissociation of apatite phase and hematite phase by fine grinding

As the grain of apatite phase is so fine and so closely wrapped with the hematite phase in the oolitic high phosphorus iron ore that fine grinding of different levels was adopted to dissociate the apatite phase and hematite phase. Firstly, by conventional mechanical crushing and screening step by step, the particles were classified into 6 groups from d_1 to d_6 by size (d_1 = 0.15 to 0.13 mm, d_2 = 0.13 to 0.11 mm, d_3 = 0.11 to 0.10 mm, d_4 = 0.10 to 0.09 mm, d_5 = 0.09 to 0.07 mm, and d_6 < 0.07 mm). Then ultrafinely ground by jet mill: particles of 0.13 to 0.15 mm were added into the grinding chamber, in which the high pressure nitrogen (≥0.6 MPa) drives the powders moving in high speed. Their mutual collision makes them tapering, and the ultrafine particles of $d_7 \le 0.01$ mm were separated by the filter separator. The distributions of Fe, P in different particles of sizes (d_1 to d_7) were analyzed by the SEM-EDS.

(2) Kinetics of gas–solid reduction

By using a Linseis Synchronous Thermal Analyser (PT 1600), the kinetics of gas–solid reduction of the high phosphorus iron ore particles were tested with particle diameters from d_1 to d_7, respectively. The experiments were carried out at 1173 K (900 °C) using high purity (99.999 pct) H_2. After that, the reduction/time curves were calculated and analyzed base on the unreacted core model *via* Eq. [1].

$$t = \frac{\rho_B r_0}{bM_B(c_{Ab} - c_{Ae})}\left\{\frac{X_B}{3k_g} + \frac{r_0}{6D_{eff}} \times \left[1 - 3(1 - X_B)^{2/3} + 2(1 - X_B)\right] + \frac{K}{k_{rea+}(1 + K)}\left[1 - (1 - X_B)^{1/3}\right]\right\}, \quad [1]$$

where ρ_B is the density of iron oxide, b is the reaction coefficient of iron oxide, M_B is the molar mass of iron oxide, d is the diameter of iron ore particles, C_{Ab} to C_{Ae} is the difference between the gas phase concentra-

Table I. Chemical Composition (Weight Percent) of the High phosphorus Iron Ore

Composition	TFe	FeO	SiO_2	CaO	Al_2O_3	MgO	P
Content	44.04	1.74	17.20	6.06	4.65	1.70	0.80

tion and reaction equilibrium concentration, k_g is the mass transfer coefficient of gas boundary layer, D_{eff} is the mass transfer coefficient of solid product layer, k_{rea+} is the interfacial reaction constant, K is the reaction equilibrium constant.

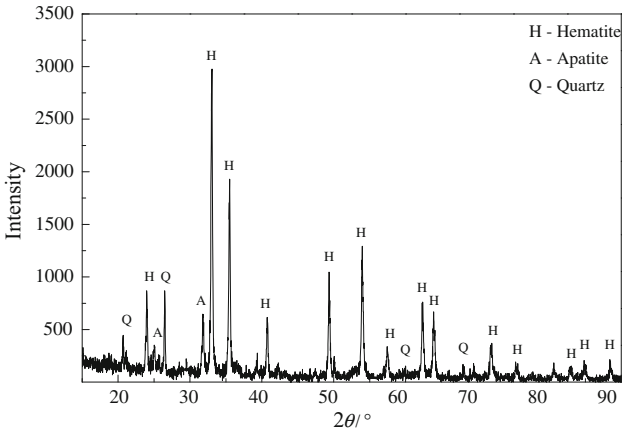

Fig. 1—XRD patterns of the high phosphorus iron ore.

(3) Gaseous reduction in a rotary furnace

The previous research on metallurgical dusts indicated that,[34] when the particle size is less than 0.01 mm, the reaction kinetic condition between particles and reducing gas in the fixed bed is poor, and the diffusion of the gas passing through the bed void takes a long time (2 hours) for ultrafine particles reduction. In order to improve the kinetic conditions of the gas–solid reaction, the contact area of reducing gas and particles should be increased, so use of fluidization has been considered. However, the research on the fluidization of different-sized particles of iron oxide in nitrogen gas flow has indicated[35] that the particles of size between 0.01 to 0.001 mm are difficult to maintain a stable fluidization state and will be blown away by the gas. Thus for treatment of ultrafine particles, a rotary furnace approach was investigated using counter-current. The ore particles in a rolling and discrete state react with the reducing gas coming from the opposite direction as illustrated in the systematic diagram of the

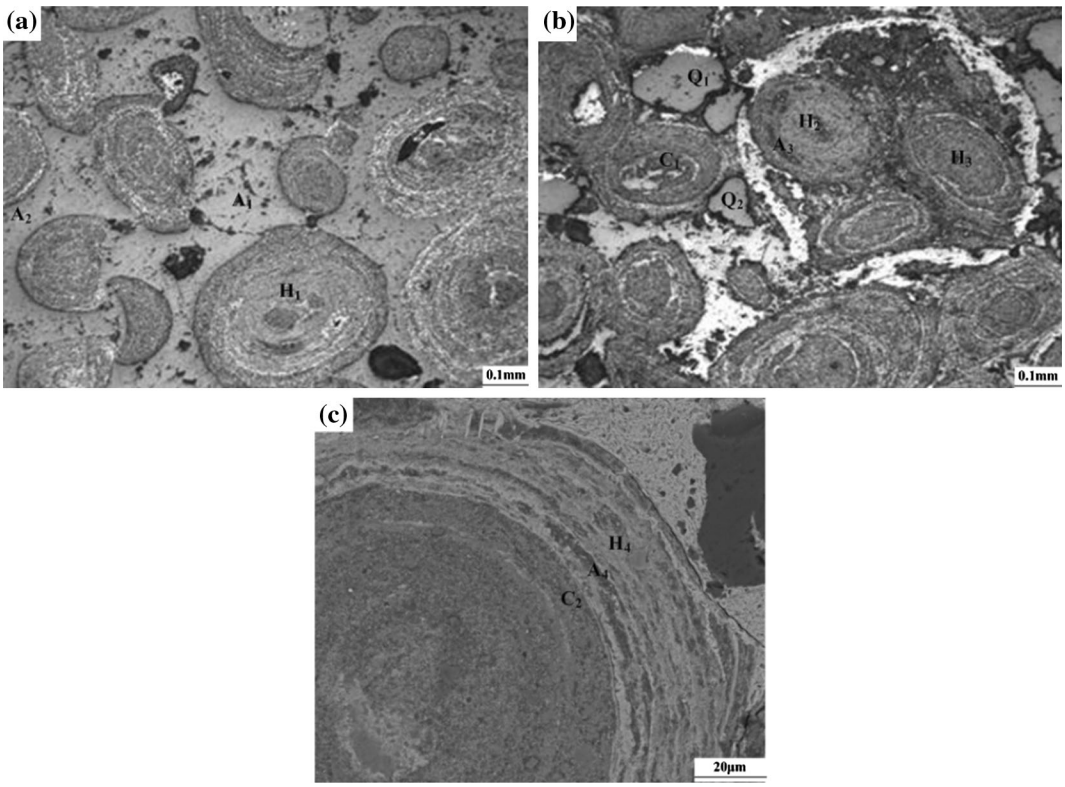

Fig. 2—Micrograph of the mineral phases.

Table II. SEM-EDS of the Mineral Phases

Position	Content of Elements/Weight Percent	Theoretical Composition
Fig. 2(a): A_1	P = 19.13, Ca = 37.08, O = 40.01, F = 1.81, Cl = 0.20	$Ca_5[PO_4]_3F$
Fig. 2(b): A_3	P = 18.97, Ca = 34.98, O = 39.03, F = 5.02	
Fig. 2(b): Q_1 Fig. 2(b): Q_2	Si = 46.00, O = 52.59 Si = 44.70, O = 52.76	SiO_2
Fig. 2(b): C_1	Al = 11.43, Si = 12.67, Fe = 38.95, O = 36.23	$Al_4[Si_4O_{10}](OH)_8$ and Fe_2O_3

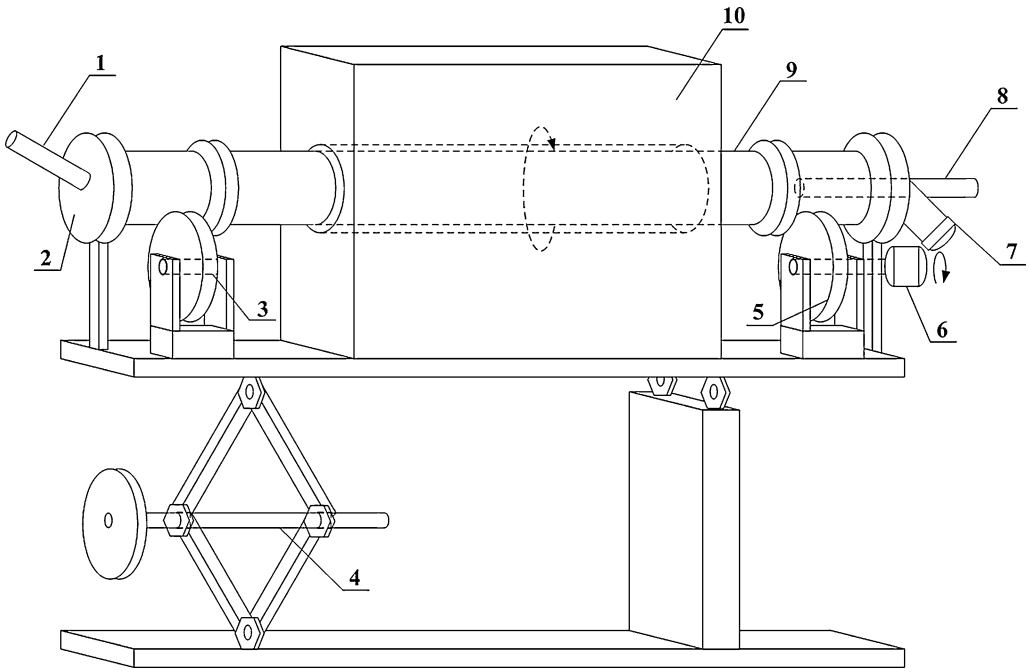

Fig. 3—Experimental equipment.

Table III. Composition of the Blast Furnace Gas

Gas	CO (pct)	CO_2 (pct)	N_2 (pct)	$\varphi_{CO} = \frac{P_{CO}}{P_{CO}+P_{CO_2}}$/pct
Original	24.0	20.1	55.9	55
Reformed	42.0	2.0	55.9	95

apparatus in Figure 3. The rotary furnace body is made of seamless steel pipe, which can effectively avoid bonding of powders to the inner wall. The length, outer diameter, and inner diameter of the furnace are 2945, 185, and 110 mm, respectively. Heating is supplied externally rather than generated by combustion of coal or gas inside the furnace, which can ensure a good reducing atmosphere in the furnace. Moreover, an adjustable speed motor and a tilting system are used to make the furnace axially rotate and radially tilt.

There were four parts during the gas–solid reduction experiment in a rotary furnace: (1) The furnace was heated to 973 K, 1073 K, 1173 K or 1273 K (700 °C, 800 °C, 900 °C or 1000 °C), respectively. (2) N_2 (flow rate is 1 m^3/h) was passed into the furnace until the air was flushed out, then the high phosphorus iron ore powders were continuously added from the feed inlet at a speed of 10 g/min. At the same time, the tilt and rotation systems were turned on to roll the particles to rolling down the tube. (3) When the material input and output achieved a balance, the N_2 was replaced with reformed blast furnace gas (the compositions of gas are shown in Table III), and the gas–solid reduction occurred in the constant temperature zone (One-third-length in the middle) of the furnace. (4) When the reduction was finished, the reduced products exited the furnace at one end and reducing exhaust at the other. After cooling to room temperature, the particle size distribution and the mass fraction of total iron (TFe) and metallic iron (MFe) in the reduction products were measured and calculated for the metallization ratio *via* Eq. [2].

$$\text{Metallization ratio} = \text{MFe pct}_{(i)}/\text{TFe pct}_{(i)}, \quad [2]$$

where MFe $pct_{(i)}$ is the mass fraction of metallic iron after reduction; TFe $pct_{(i)}$ is the mass fraction of total iron after reduction.

(4) Magnetic separation of the reduction products

After the reduction experiments, the reduction products of the high phosphorus iron ore powder in different sizes (d_1 to d_7) were further separated by a magnetic tube: the reduction products mixed with water were added into magnetic tube and adjusted to the specified magnetic flux density of 100 mT, and then the magnetic products and non-magnetic products mixed with water were obtained, respectively. After that, the two products were further filtrated and dried, and the mass fractions of Fe and P in the two isolated products were measured.

III. RESULTS AND DISCUSSION

A. *Relationship Between the Dissociation and Fine Grinding*

The SEM-EDS images of the ore particles in different sizes (d_1 to d_7) are shown in Figure 4, and the mass

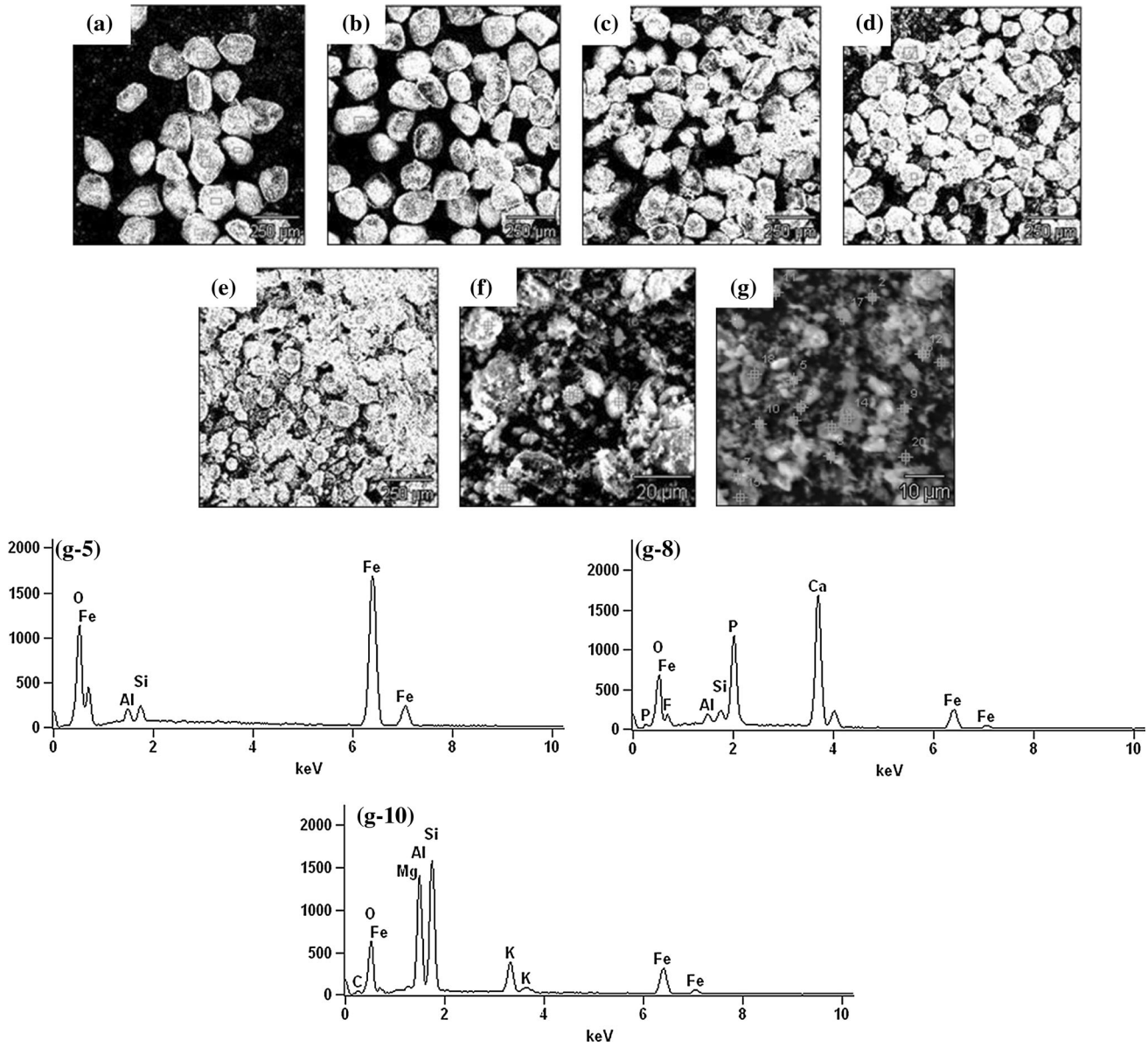

Fig. 4—SEM-EDS images of high phosphorus iron ore particles in different sizes.

fractions of Fe and P of the particles evaluated from EDS analysis are shown in Figure 5. By mechanical crushing (for particle of d_1 to d_5 = 0.15 to 0.07 mm), it is almost impossible to dissociate the apatite phase and hematite phase, and the mass fractions of P in different particles are maintained between 0.60 and 1.10 wt pct while that of Fe are between 43.0 and 61.00 wt pct. When the ores are further ground to $d_6 < 0.07$ mm, it becomes apparent that in rich Fe particle P is less than 0.20 wt pct, and in P rich particles P is more than 1.90 wt pct. Furthermore, by grinding the ore using the jet mill to d_7 = 0.01 to 0.001 mm, it is obvious that the distributions of P and Fe are nonuniform in different particles. Among them, the mass fraction of Fe in particles 5, 11, 12, and 15 is more than 61.59 wt pct with almost no detectable P elements, so they are typical hematite particles; the mass fraction of P in particles 1, 3, 8, 9, 13, and 18 is up to 7.28 to 12.00 wt pct, while that of Fe is only 9.36 to 33.30 wt pct, so they are typical apatite particles; In addition, the mass fractions of Fe and P in particles 4, 10, and 16 are both low, and they are typical gangue particles that are mainly composed of Si, Al, and Mg. Consequently, grinding the high phosphorus iron ore to 0.001 to 0.0001 mm using the jet mill can realize the great dissociation of apatite phase and hematite phase.

B. *Effect of Particle Size on Intrinsic Kinetics of Gas–Solid Reduction*

The reduction/time curves of high phosphorus iron ores in different sizes (d_1 to d_7) are shown in Figure 6(a). Based on the unreacted core model the reduction resistance of external diffusion in the gas boundary

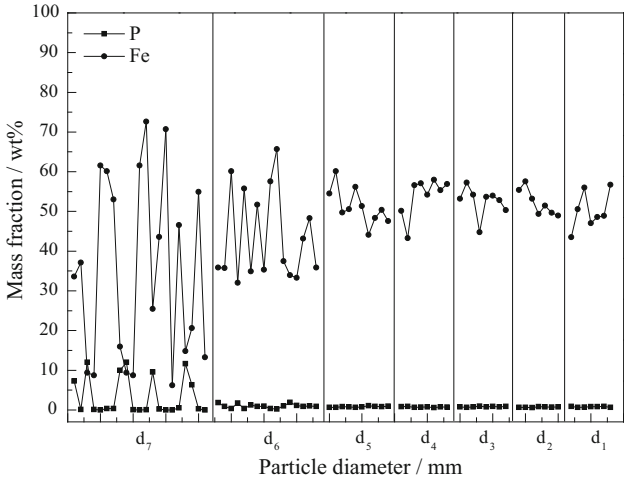

Fig. 5—Mass fractions of Fe and P of the particles evaluated from EDS analysis.

layer, internal diffusion in the solid product layer, and interfacial chemical reaction was analyzed *via* Eqs. [3] through [5], with the results shown in Figure 6(b). It is apparent that the complete reaction time decreases with the decrease of particle size, meanwhile the resistance of external and internal diffusions also decreases with the decrease of particle size. When the particle diameter is reduced to 0.01 to 0.001 mm, the complete reaction time is only 100 seconds, and the gas–solid reduction is limited by interfacial chemical reaction, while the mass transfer in the gas boundary layer and solid product layer is not rate limiting step in the reduction process.

$$\eta_{\mathrm{d}}=\frac{1}{k_{\mathrm{g}}}=\frac{d}{(2.0+0.6Re^{\frac{1}{2}}Sc^{\frac{1}{3}})\,D} \qquad [3]$$

$$\eta_{\mathrm{i}}=\frac{r_0(r_0-r_{\mathrm{i}})}{D_{\mathrm{eff}}\cdot r_{\mathrm{i}}}=\frac{r_0(1-X_B)^{-1/3}-r_0}{D_{\mathrm{eff}}} \qquad [4]$$

$$\eta_{\mathrm{c}}=\frac{K}{k_{\mathrm{rea}}+(1\ +\ \mathrm{K})}\frac{r_0^2}{r_{\mathrm{i}}^2}=\frac{K}{k_{\mathrm{rea}+}(1+K)}(1-X_{\mathrm{B}})^{-2/3} \qquad [5]$$

where n_{d} is the resistance of external diffusion, n_{i} is the resistance of internal diffusion, n_{c} is the resistance of interface reaction, X_{B} is the reduction degree, r is the radius of ore particles, k_{g} is the mass transfer coefficient of gas boundary layer, D_{eff} is the mass transfer coefficient of solid product layer, $k_{\mathrm{rea}+}$ is the interfacial reaction constant, K is the reaction equilibrium constant.

C. *Rotating Furnace Reduction*

(1) Effect of particle size on gaseous reduction

The tests of powder's motion behavior at 1173 K (900 °C) were carried out using high phosphorus iron ores in different sizes (d_1 to d_7), and the reduction times for the powders going through the constant temperature

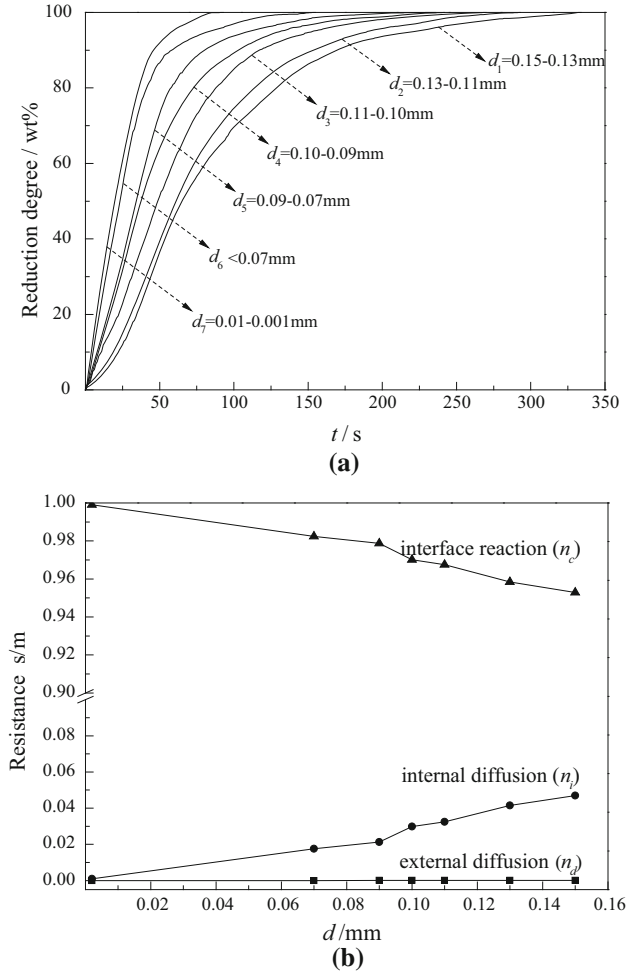

Fig. 6—Intrinsic kinetics of gas–solid reduction.

zone of the furnace are shown in Figure 7(a). It can be seen that by fixing the rotation speed to 2.5 rpm, and adjusting the furnace body angle to 1, 2, 3, 4, and 5 deg, the reduction times of ultrafine ore powders (d_7) were controlled to be 16.7, 13., 10.0, 6.7, and 4.3 minutes, respectively. In the same conditions of the rotation speed and the furnace body angle, the reduction time decreases with the decrease of particle size as shown in Figure 7(a) (solid lines). In order to investigate the iron ores of different sizes reduced for the same time, the furnace body angle of iron ores in size d_6 to d_1 was increased by 0.1 to 0.8 deg over that of d_7 as shown in Figure 7(a) (dash lines). Consequently, the reduction experiments of iron ores in different sizes (d_1 to d_7) were carried out at 1173 K (900 °C) for 4.3, 6.7, 10.0, 13.3, and 16.7 minutes, respectively, with the results shown in Figure 7(b). The reaction rate increases significantly with the decrease of particle size, and the metallization ratio of ultrafine powders (d_7) can reach 83.91 to 97.32 pct after reduced for 4.3 to 16.7 minutes, while that of powders with the size of 0.13 to 0.15 mm (d_1) is only 33.24 to 40.22 pct. The main reasons are that in the rotating inclined reactor, the particles react with the reducing gas coming from the opposite direction in a rolling and discrete state, which greatly increases the

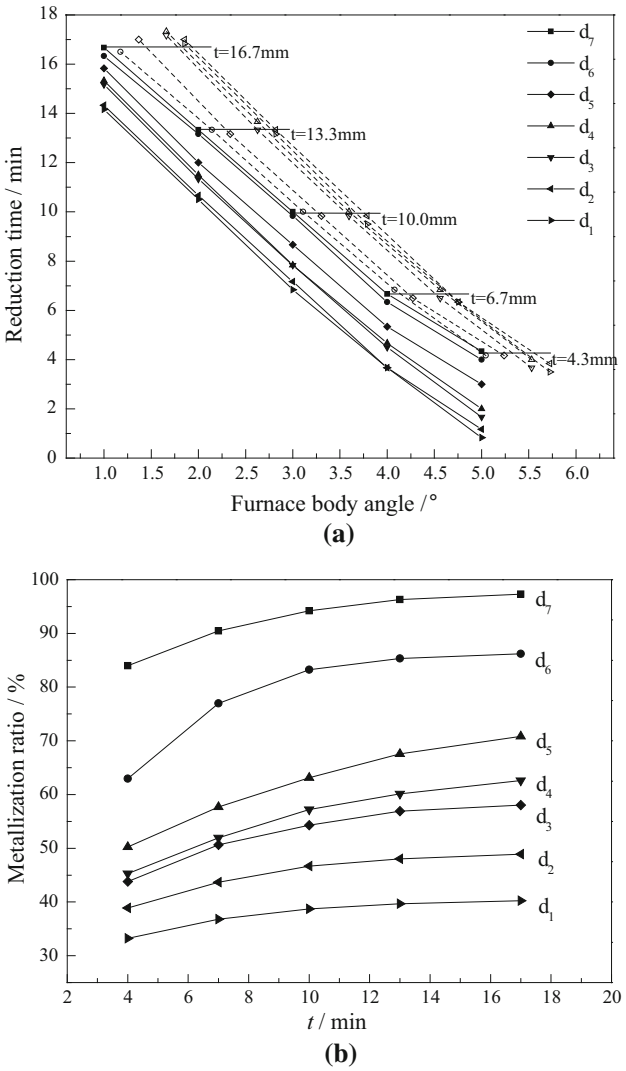

Fig. 7—Effect of particle size on gaseous reduction in a rotary furnace.

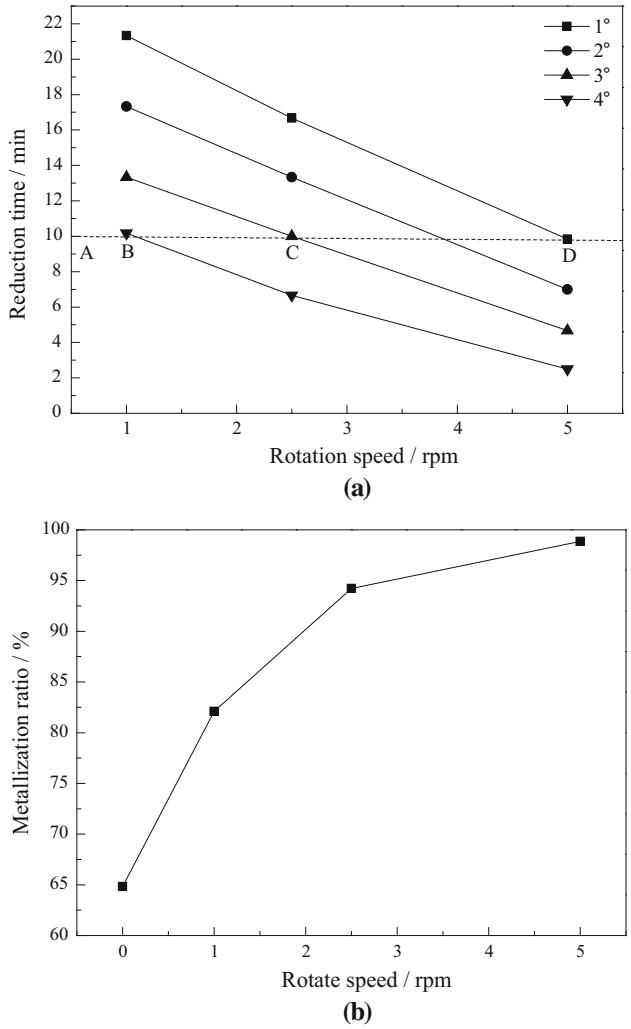

Fig. 8—Effect of rotation speed on gaseous reduction of ultrafine ore in a rotary furnace.

contact area and improves the kinetic conditions. Hence, with the decrease of particle size, the inner diffusion resistance of the reducing gas in solid product layers decreases, while the contact interface area of gas–solid reaction increases.

(2) Effect of contact state of ultrafine ore and reducing gas on gaseous reduction

The tests of motion behavior of ultrafine powders (d_7) at 1173 K (900 °C) were further carried out by adjusting the rotation speed to 1.0, 2.5 and 5.0 rpm, respectively, with the reduction times shown in Figure 8(a). It can be seen that the reduction time decreases with the increase of the rotation speed. In order to investigate the ultrafine iron ore reducing in different rotation speeds for the same time of 10 minutes, the furnace body angles were adjusted to 4, 3, and 1 deg in the rotation speed of 1.0, 2.5 and 5.0 rpm, respectively (see the points B, C, and D in Figure 8(a)). Consequently, 3 groups of reduction experiments in rotating state with the above conditions were carried out; simultaneously, the reduction experiment in static state of equivalent ore was carried out for the same time as a parallel experiment, with the results shown in Figure 8(b). It is obvious that the metallization ratio of iron ore after static reduction for 10 minutes is only 66.68 wt pct, while it can reach 82.10 to 98.86 wt pct by reducing in rotating state for the same time. Furthermore, the metallization ratio increases significantly with the increase of the rotation speed. Moreover, it can be further seen from the morphology of the reduction products as shown in Figures 9(a) and (b), the product's color is uniformly ash black after the reduction in rotating state, while the product's color appears as obvious stratification after the reduction in static state, with the upper ash black and the bottom black or red brown. According to the XRD analyses shown in Figure 9(c), it is a further evidence that the Fe in the upper part is almost reduced to metal Fe after static reduction, while in the bottom part it remains in the form of hematite. The differences that occurred in the upper and bottom of the reduction products obtained by static reduction were caused by the too small pores among the particles of the ultrafine

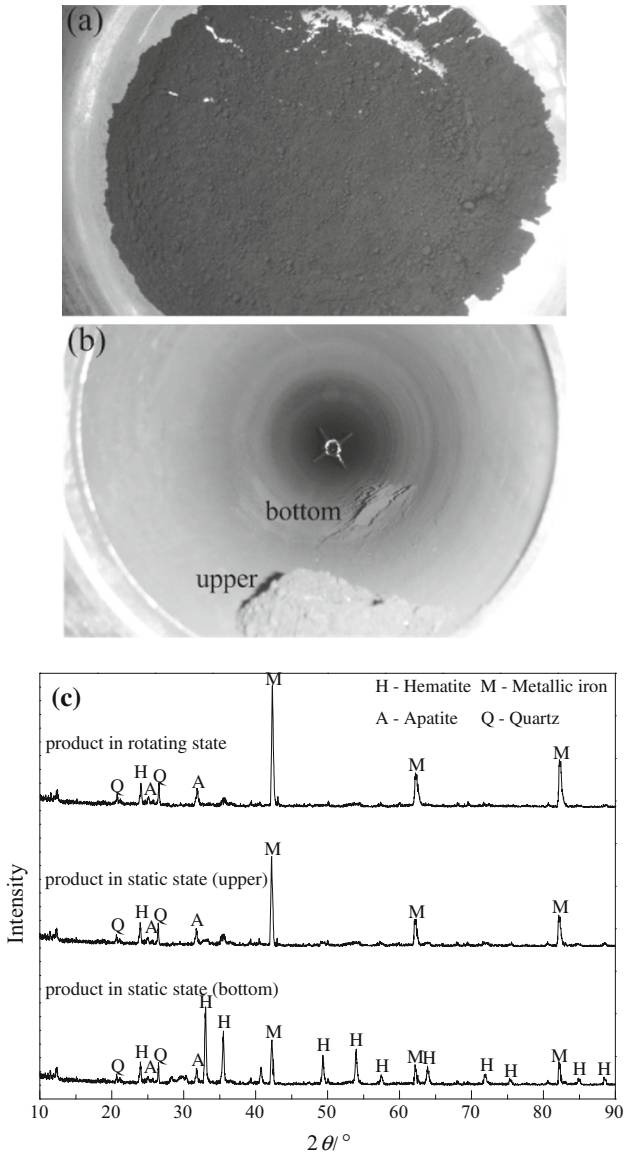

Fig. 9—Morphology and the mineral phase of the reduction products.

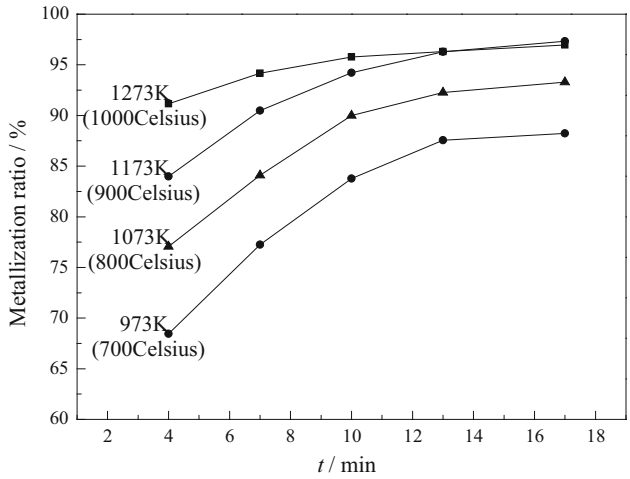

Fig. 10—Effect of temperature on gaseous reduction of ultrafine ore in a rotary furnace.

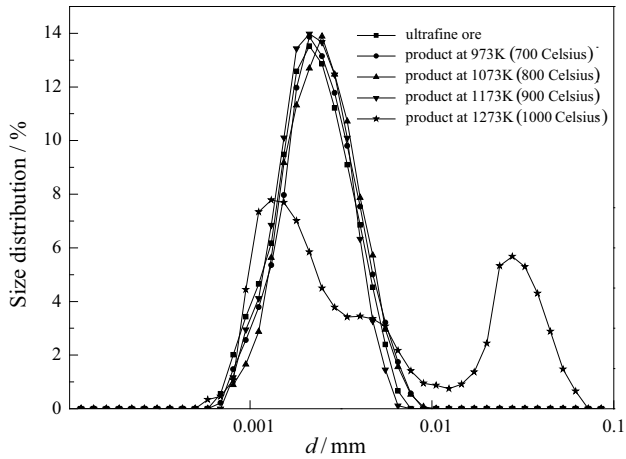

Fig. 11—Particle size distribution of the reduction products.

powders; in the static state, they hinder the diffusion of reducing gas to bottom powders, thereby limiting the gas–solid reaction rate. While in the rotating state particles are disturbed by the reactor, the discrete particle and the reducing gas can fully contact, which avoids the resistance of gas diffusion among the particles. Hence, when the rotation speed increases, the particle moves more intensely and more discretely, and the contact chance of particles and reducing gas is further increased.

(3) Effect of temperature on gaseous reduction of ultrafine ore

The results of reduction experiments in rotary furnace of ultrafine iron ore at 973 K, 1073 K, 1173 K and 1273 K (700 °C, 800 °C, 900 °C and 1000 °C) are shown in Figure 10, and the particle sizes distribution of reduction products are shown in Figure 11. It can be seen that as the temperature rises from 973 K to 1173 K (700 °C to 900 °C), the average metallization ratio increases by 5.70 pct for an increase 100 °C. This can be explained as, with the increasing of temperature, both the diffusion coefficient and the reaction rate constant increase, which improve the kinetic conditions of the gas–solid reaction. Compared with the particle size distribution of original iron ore, the reduced particles still maintained their original sizes, and there is no sintering phenomenon and iron whisker growth in the products reduced at 973 K to 1173 K (700 °C to 900 °C). The reason is that the iron ore particles react with reducing gas in a rolling state at sub-melting point temperatures, and the turbulence in the furnace effectively prevents the produced metallic iron particles from aggregating, which prevents the P, S, and other impurity elements from infiltrating into iron matrix. However, compared to the reduction at 973 K to 1173 K (700 °C to 900 °C), the metallization ratio at 1273 K (1000 °C) slowly increases with the increase of reduction time, and the sintered pellets begin to appear in the reduction product, which prevents the diffusion of the gas.

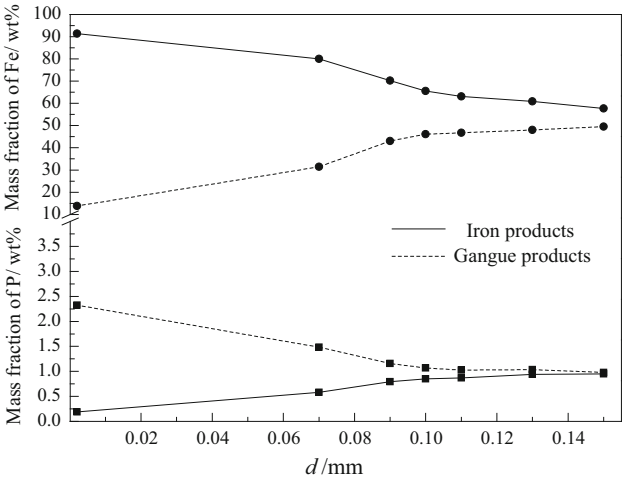

Fig. 12—Magnetic separation results of the reduction products.

D. *Magnetic Separation of the Reduction Products*

After reduction in a rotary furnace at 1173 K (900 °C) for ~17 minutes, magnetic separation of the reduction products was further carried out, with the results shown in Figure 12. For the high phosphorus iron ore in size of 0.15 to 0.07 mm (d_1 to d_5), it is impossible to separate Fe phase, and the mass fraction of Fe in iron products is 57.69 to 70.28 wt pct while it is still 43.05 to 49.49 wt pct in gangue products. As for the ore in a size of less than 0.07 mm (d_6), the well-separation of the Fe phase in the iron and gangue products occurs, and the mass fraction of Fe in iron products is up to 80.07 wt pct while it is 31.45 wt pct in gangue products; simultaneously, a little separation of the P phase occurs, and the mass fraction of P in iron products is decreased to 0.58 wt pct while it is 1.48 wt pct in gangue products. When it comes to the ultrafine ore (d_7), the great separation of the Fe and P in the iron and gangue products occurs, and in the iron products the mass fraction of Fe is up to 91.42 wt pct and P is only 0.19 wt pct, while in the gangue products the mass fraction of Fe is decreased to 13.77 wt pct and for P 2.32 wt pct.

IV. CONCLUSIONS

It was confirmed by the experiment results that separating of P phase and Fe phase in phosphorus oolitic iron ore by ultrafine grinding and gaseous reduction in a rotary furnace was an effective method.

By using the jet mill to ground the high phosphorus iron ore to ultrafine 0.01 to 0.001 mm, the great dissociation of apatite phase and hematite phase was realized.

By the way of gaseous reduction in a rotary furnace at sub-melting point temperatures, the ore particles in a rolling and discrete state react with the reducing gas coming from the opposite direction. In this process, the reaction rate increases significantly with the decrease of particle size, and the metallization ratio of ultrafine high phosphorus iron ores can reach 83.91 to 97.32 pct, but only 33.24 to 40.22 pct for powders with the size of 0.13 to 0.15 mm.

Due to the rotating furnace reduction at sub-melting point temperatures, the reduced particles still maintained their original sizes, without the presence of sintering phenomenon or iron whisker. Hence, the iron products with 91.42 wt pct of Fe and 0.19 wt pct of P, and the gangue product with 13.77 wt pct of Fe and 2.32 wt pct of P were easily obtained by magnetic separation.

ACKNOWLEDGEMENT

The authors like to thank the support from the Chinese Natural Science Foundation (No. 51234001 and No. 51404025) and the Fundamental Research Funds for the Central Universities (FRF-TP-14-010A1).

REFERENCES

1. J.T. Yu, Z.C. Guo, and H.Q. Tang: *ISIJ Int*., 2013, vol. 53, pp. 2056–64.
2. X.Y. Hao, H.X. Dai, and Z.Q. Zhao: *Met Mine*, 2007, vol. 1, pp. 7–12.
3. C.Y. Cheng, V.N. Misra, J. Clough, and R. Mun: *Miner. Eng*., 1999, vol. 12, pp. 1083–92.
4. E. Matinde and M. Hino: *ISIJ Int*., 2011, vol. 51, pp. 220–7.
5. E. Matinde and M. Hino: *ISIJ Int*., 2011, vol. 51, pp. 544–51.
6. G.W. Qi, A. Parentich, and L.H. Little: *Int. J. Miner. Process*., 1992, vol. 34, pp. 83–102.
7. H. Han, D. Duan, P. Yuan, and S. Chen: *Ironmak. Steelmak*., 2014, vol. 000, pp. 01–06.
8. M. Omran, T. Fabritius, N. Abdel-Khalek, M. El-Aref, A.E.-H. Elmaniwi, M. Nasr, and A. Elmahdy: *J. Miner. Mater. Charact. Eng*, 2014, vol. 2, pp. 414–27.
9. M. Omran, T. Fabritius, and R. Mattila: *Powder Technol*., 2015, vol. 269, pp. 7–14.
10. M. Omran, T. Fabritius, N. Abdel-Khalek, and A. Elmahdy: *Sep. Purif. Technol*., 2014, vol. 136, pp. 223–232.
11. M. Omran, T. Fabritius, N. Abdel-Khalek, and A. Elmahdy: *Appl. Surf. Sci*., 2015, vol. 345, pp. 127–140.
12. A.P.L. Nunes, C.L.L. Pinto, G.E.S. Valadao, and P.R.M. Viana: *Miner. Eng*., 2012, vol. 39, pp. 206–212.
13. R.C. Guimaraes, A.C. Araugo, and A.E.C. Peres: *Miner. Eng*., 2005, vol. 18, pp. 199–204.
14. P. Delvasto, A. Ballester, J.A. Munoz, F. Gonzalez, M.L. Blazquez, J.M. Igual, and C.G. Balboa: *Miner. Eng*., 2009, vol. 22, pp. 01–09.
15. O. Priha, T. Sarlin, P. Blomberg, L. Wendling, J. Makinen, M. Arnold, and P. Kinnunen: *Hydrometallurgy*, 2014, vol. 150, pp. 269–75.
16. T.M. Bhatti and W. Yawar: *Hydrometallurgy*, 2010, vol. 103, pp. 54–9.
17. P. Delvasto, A. Valverde, A. Ballester, J.A. Munoz, F. Gonzalez, M.L. Blazquez, J.M. Igual, and C. Garcia-Balboa: *Hydrometallurgy*, 2008, vol. 92, pp. 124–129.
18. W.T. Xia, Z.D. Ren, and Y.F. Gao: *J. Iron Steel Res. Int*., 2011, vol. 18, pp. 01–04.
19. Y. Zhang and M. Muhammed: *Hydrometallurgy*, 1989, vol. 21, pp. 255–275.
20. Y.S. Jin, T. Jiang, Y.B. Yang, L. Qian, L.G. Hui, and G.Y. Feng: *J. Cent. South Univ. Technol*., 2006, vol. 13, pp. 673–677.
21. M.J. Fisher-White, R.R. Lovel, and G.J. Sparrow: *ISIJ Int*., 2012, vol. 52, pp. 1794–1800.
22. M.J. Fisher-white, R.R. Lovel, and G.J. Sparrow: *ISIJ Int*., 2012, vol. 52, pp. 797–803.

23. K. Ionkov, S. Grydardzhiev, A.C. de Araujo, D. Bastin, and M. Lacoste: *Miner. Eng.*, 2013, vols. 46–47, pp. 119–27.
24. Y.L. Li, T.C. Sun, A.H. Zou, and C.Y. Xu: *Int. J. Min. Sci. Technol.*, 2012, vol. 22, pp. 323–8.
25. C.Y. Xu, T.C. Sun, J. Kou, Y.L. Li, X.L. Mo, and L.G. Tang: *Trans. Nonferrous Met. Soc. China*, 2012, vol. 22, pp. 2806–12.
26. K.Q. Li, W. Ni, M. Zhu, M.J. Zheng, and Y. Li: *J. Iron Steel Res.*, 2011, vol. 18, pp. 9–13.
27. S.J. Bai, S.M. Wen, D.W. Liu, W.B. Zhang, and Q.B. Cao: *ISIJ Int.*, 2012, vol. 52, pp. 1757–63.
28. W. Yu, T.C. Sun, J. Kou, Y.X. Wei, C.Y. Xu, and Z.Z. Liu: *ISIJ Int.*, 2001, vol. 53, pp. 427–33.
29. Z.L. Zhao, H.Q. Tang, and Z.C. Guo: *J. Iron Steel Res.*, 2013, vol. 20, pp. 16–24.
30. H.Q. Tang, Z.C. Guo, and Z.L. Zhao: *J. Iron Steel Res.*, 2010, vol. 17, pp. 01–06.
31. Z.L. Zhao, H.Q. Tang, and Z.C. Guo: *J. Univ. Sci. Technol. Beijing*, 2009, vol. 31, pp. 964–9.
32. H.Q. Tang, D.W. Liu, H.Y. Zhang, and Z.C. Guo: *Metall. Mater. Trans. B*, 2014, vol. 45B, pp. 1683–94.
33. S. Fukagai, T. Hamano, and F. Tsukihashi: *ISIJ Int.*, 2007, vol. 47, pp. 187–9.
34. J.T. Gao, S.Q. Li, and Y.L. Zhang: *Ironmak. Steelmak.*, 2012, vol. 39, pp. 446–53.
35. J.T. Gao: *Steel Res. Int.*, 2014, vol. 85, pp. 616–22.